BAMS Article

A Review

Anomaly-Based versus Full-Field-Based Weather Analysis and Forecasting

Weihong Qian, Jun Du, and Yang Ai

ABSTRACT: Comparisons between anomaly and full-field methods have been carried out in weather analysis and forecasting over the last decade. Evidence from these studies has demonstrated the superiority of anomaly to full field in the following four aspects: depiction of weather systems, anomaly forecasts, diagnostic parameters, and model prediction. To promote the use and further discussion of the anomaly approach, this article summarizes those findings. After examining many types of weather events, anomaly weather maps show at least five advantages in weather system depiction: 1) less vagueness in visually connecting the location of an event with its associated meteorological conditions, 2) clearer and more complete depictions of vertical structures of a disturbance, 3) easier observation of time and spatial evolution of an event and its interaction or connection with other weather systems, 4) simplification of conceptual models by unifying different weather systems into one pattern, and 5) extension of model forecast length due to earlier detection of predictors. Anomaly verification is also mentioned. The anomaly forecast is useful for raising one's awareness of potential societal impact. Combining the anomaly forecast with an ensemble is emphasized, where a societal impact index is discussed. For diagnostic parameters, two examples are given: an anomalous convective instability index for convection, and seven vorticity and divergence related parameters for heavy rain. Both showed positive contributions from the anomalous fields. For model prediction, the anomaly version of the beta-advection model consistently outperformed its full-field version in predicting typhoon tracks with clearer physical explanation. Application of anomaly global models to seasonal forecasts is also reviewed.

KEYWORDS: Operational forecasting; Climatology; Anomalies

https://doi.org/10.1175/BAMS-D-19-0297.1

Corresponding author: Prof. Weihong Qian, qianwh@pku.edu.cn

In final form 10 December 2020

AFFILIATIONS: **Qian**—Guangzhou Institute of Tropical and Marine Meteorology, and Guangdong Provincial Key Laboratory of Regional Numerical Weather Prediction, CMA, Guangzhou, and Department of Atmospheric and Oceanic Sciences, Peking University, Beijing, China; **Du**—NOAA/NCEP/Environmental Modeling Center, College Park, Maryland; **Ai**—Department of Atmospheric and Oceanic Sciences, Peking University, Beijing, China

The first weather chart was drawn by German meteorologist H. W. Brandes in 1819 using weather reports collected in 1783. The first daily weather map was plotted based on telegraphic reports in the United States in 1849. Using radio technology to transmit meteorological information promoted the real-time usability of weather charts after World War I. Upper air weather charts were developed after the invention of radiosonde technologies in World War II (Grahame 2000). Since then, three-dimensional weather systems can be described by using the full fields (or total variables) of geopotential height, air temperature, specific humidity and wind (both direction and speed). These full-field-based maps are referred to "traditional" or "conventional" weather maps (charts) in this paper. Numerical weather prediction (NWP) model forecasts are also commonly analyzed and displayed in the form of conventional weather maps. However, traditional weather maps have limitations. Since the weather disturbance signal is much smaller than the background climate, the important detailed information of a weather disturbance is often hidden (too weak to show) and overlooked in a conventional weather chart. In contrast, an anomaly field (i.e., a departure from climate) is found to be more directly associated with a local weather event than a full field (Qian et al. 2016b). This situation is illustrated by Fig. 1, where the two "positive" events and one "negative" event are hardly visible in the full field but clearly revealed in the anomaly.

To explore the added value (i.e., in addition to the value of convectional weather charts) of the anomaly approach in weather analysis and forecasting, an anomaly-based method has been systematically compared with the full-field-based method over the last decade. The study was motivated by an extremely severe freezing rain event that happened in southern China in January 2008. The question to be answered was whether this freezing rain could be predicted by using any signal for the leading 5 days, where an anomaly method has been employed (Qian and Zhang 2012). After that, the study was greatly expanded into many other weather extremes including heat waves, cold surges, heavy rainfall, convective storms (tornado and hail), tropical cyclones, fire weather, and fog as well as air pollution episodes (haze). The findings have been documented in more than 30 journal articles. These studies have consistently

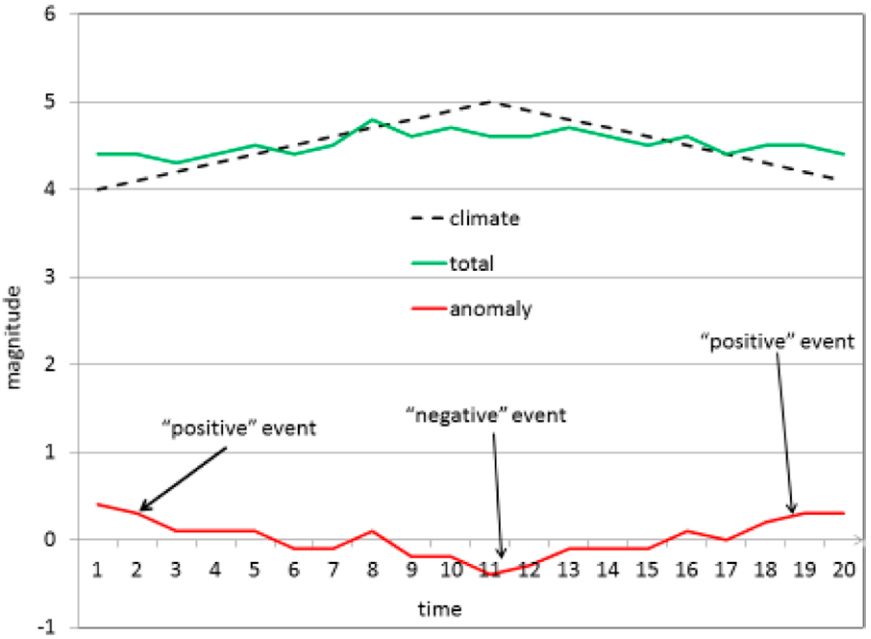

Fig. 1. A schematic diagram of converting a total variable or full field (green curve) into an anomaly (red curve) by removing climatic component (black dash line) to better reveal hidden anomalous weather episodes, where two "positive" and one "negative" anomalous events are shown.

demonstrated the superiority of the anomaly approach to the full-field approach. Besides these studies, anomaly forecasts have also gained forecaster attention in short range weather forecasting in the last two decades (Grumm and Hart 2001; Junker et al. 2008, 2009; Graham and Grumm 2010; Grumm 2011a,b; Du et al. 2013). To promote the anomaly-based approach, this article will summarize and review those findings (primarily from the authors' past work) for the community to discuss further. It will be presented from the following four angles: description of weather systems ["Anomaly weather map (charts)" section], anomaly forecasts ("Anomaly forecast" section), diagnostic parameters ("Diagnostic parameters" section), and model predictions ("Model prediction" section). The anomaly method is described in the second section. A summary is given in the fourth section.

Anomaly-based approach

Similar to the monthly mean variable decomposition done by Peixoto and Oort (1992), a daily mean total variable can be decomposed into four components: zonally mean symmetric and asymmetric climates as well as zonally mean symmetric and asymmetric anomalies (Qian 2012a,b). The poleward propagation of zonally mean symmetric anomalous flow is associated with polar oscillations in intraseasonal and interannual scales, while the asymmetric anomaly is associated with regional oscillations (Qian and Liang 2012). Since both the asymmetric climate and symmetric anomaly are negligible for daily synoptic-scale motions, they later simply decomposed the daily mean or hourly variable into two parts: climate and anomaly for weather analysis and forecasting (same as Fig. 1). Therefore, the words "climate" and "anomaly" in this study referred to an hourly time scale rather than monthly or seasonal mean used in climate study.

Hourly climatology can be estimated by averaging reanalysis data for a variable υ at time t (24 h a day) on calendar date d over M years,

$$\tilde{\upsilon}_d(\lambda,\phi,p,t)=\sum_{y=1}^{M}\upsilon_{(d,y)}(\lambda,\phi,p,t)/M, \tag{1}$$

where year y runs from 1 to M ($M \geq 30$ years), while λ, ϕ, and p denote longitude, latitude. and pressure level, respectively. When M is large enough, the estimated climatology should be a static state under thermodynamic equilibrium of the Earth-atmosphere system, which is only forced by the solar radiation and surface conditions (Qian 2017). The hourly climatology contains the diurnal cycle and the annual cycle. In this study, the ERA-Interim reanalysis data (Dee et al. 2011) are used with M = 30 years (1981–2010), which are available four times per day at 6-h intervals. Once the climatology is known, an anomaly $\upsilon'_{(d,y)}(\lambda, \varphi, p, t)$ can be extracted from a total variable $\upsilon_{(d,y)}(\lambda, \varphi, p, t)$ by subtracting climatology $\tilde{\upsilon}_{(d,y)}(\lambda, \varphi, p, t)$ using Eq. (2):

$$\upsilon_{(d,y)}(\lambda,\varphi,p,t)=\tilde{\upsilon}_d(\lambda,\varphi,p,t)+\upsilon'_{(d,y)}(\lambda,\varphi,p,t). \tag{2}$$

Figure 2 gives an illustration of this decomposition for the 300-hPa geopotential height (GPH) and temperature at 0000 UTC 28 April 2011. The total variables or full fields are shown in Fig. 2a, where there are both zonal waves along latitudes and vortices with circled GPH centers, such as a vortex (V1) in northeast China and a vortex (V2) on the west coast of North America. The corresponding climatology of GPH and temperature is shown in Fig. 2c, along with the wind climatology shown in Fig. 2b. On the climatological fields, there are only waves zonally along latitudes with no local vortices. These waves are atmospheric tides which are forced by solar radiation and surface characteristics as well as solar and lunar gravitation. Although the climatology might have a small change in the long-term trend (at decadal or longer scales) forced

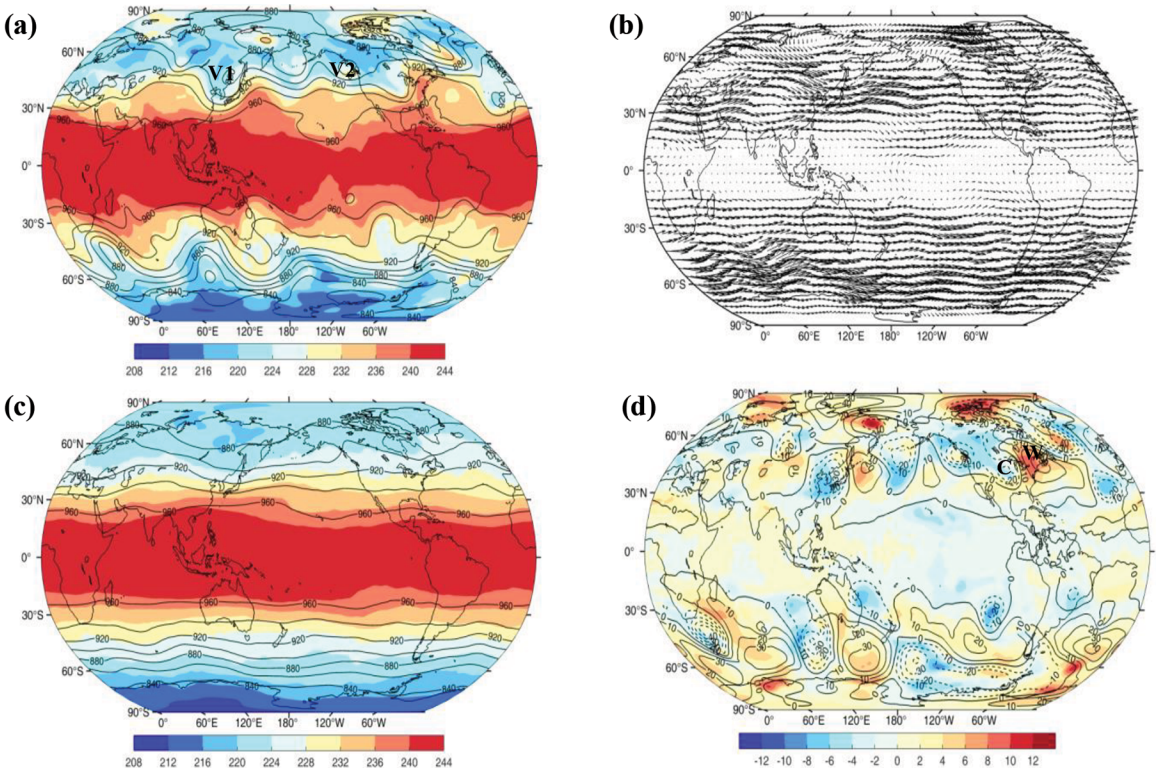

Fig. 2. (a) Total height $H_{\{d,y\}}(\lambda, \varphi, t)$ (solid contour, 20 × 10-gpm interval) , and total temperature $T_{\{d,y\}}(\lambda, \varphi, t)$ (shading, 4-K interval) ; (b) climatological winds $\tilde{v}(\lambda, \varphi, t)$ (m s^{-1}); (c) climatological height $H(\lambda, \varphi, t)$, and climatological temperature $T(\lambda, \varphi, t)$; and (d) height anomaly $H'_{\{d,y\}}(\lambda, \varphi, t)$ (contour, 10 × 10-gpm interval) and temperature anomaly $T'_{\{d,y\}}(\lambda, \varphi, t)$ $T_{\{d,y\}}(\lambda, \varphi, t)$ (red–yellow shading for positive and blue shading for negative, 1-K interval) at 300 hPa at 0000 UTC 28 Apr 2011 using the ERA-Interim data. Letters "V1" and V2 indicate a vortex in (a). Letters "W" and "C" are warm and cold centers of temperature anomalies in (d).

by solar radiation intensity fluctuation and human activity, this small trend change should have little impact on anomalous signals related to daily weather disturbances on an anomaly weather map. Unlike climatology, the anomaly map (Fig. 2d) shows mainly local vortices (GPH and temperature anomalies) but rarely zonal waves. There are many positive and negative centers of GPH and temperature anomalies, particularly in extratropical regions. For instance, in the central United States there was a cold/low center (C) while in the eastern United States there was a warm/high center (W). These anomalies were associated with a severe tornadic storm in the southern United States (Qian et al. 2019b; as well as Fig. 14 below). These cold and warm centers as well as low (vortex) and high (antivortex) centers reflect not only temperature and pressure anomalies but also wind anomalies, because these anomalous systems satisfy the geostrophic balance horizontally and the hydrostatic balance vertically (Chen et al. 2017; Qian et al. 2016d,e).

It is the anomalous systems (as shown in Fig. 2d) that need to be focused on and predicted in daily weather analysis and forecasting, since the climatology (as shown in Figs. 2b,c) is fixed and known.

Superiority of anomaly to full-field approach

Anomaly weather map (charts). The term "weather map" in this study is a general one, and not only refers to a two-dimensional horizontal chart but any charts (such as vertical cross section) of meteorological variables. Five advantages of anomaly weather maps over conventional weather maps are demonstrated in this section. First, it is easier or less vague to visually connect the location of a weather event with associated meteorological conditions

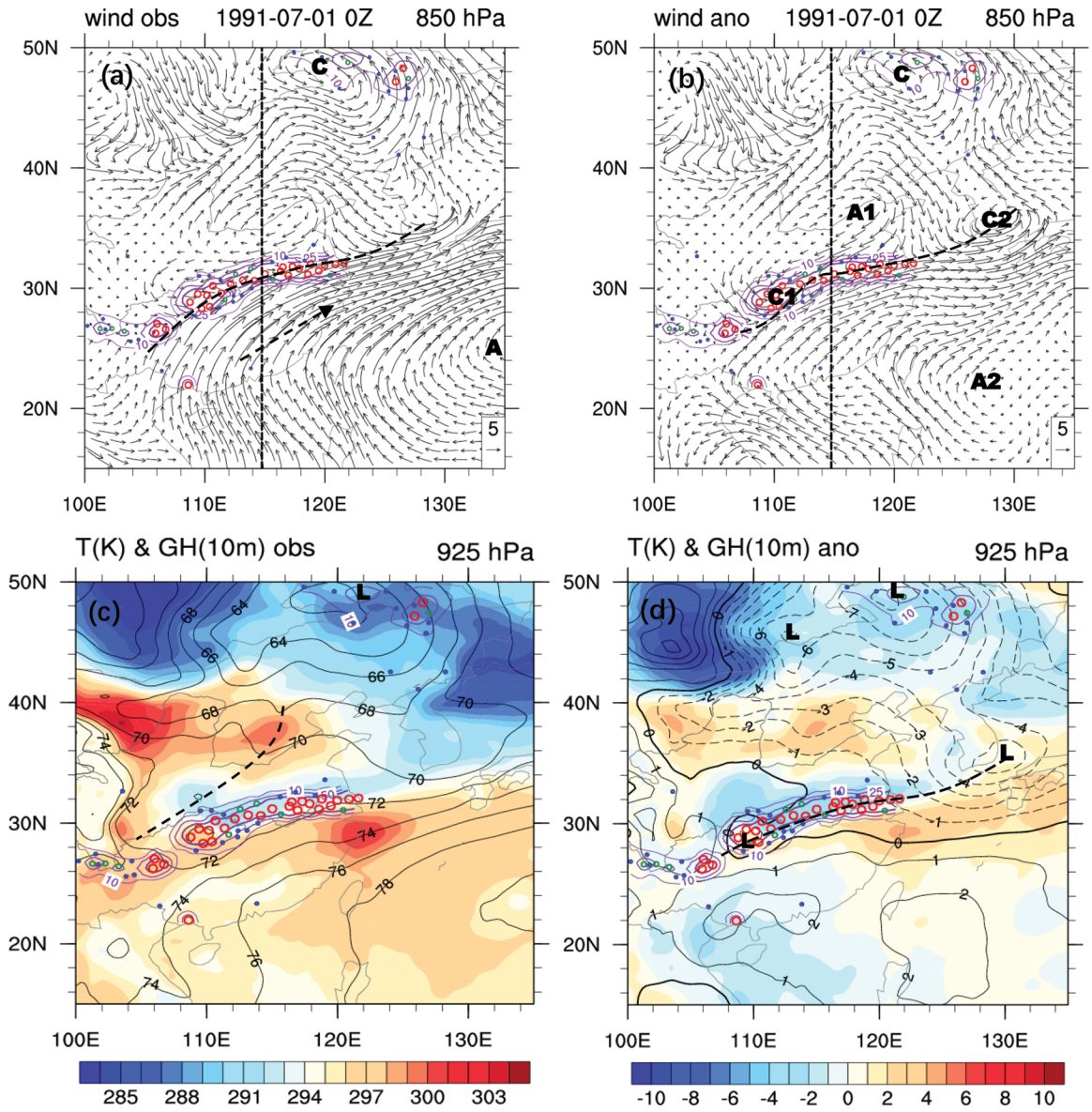

Fig. 3. (a) Total and (b) anomalous winds (m s^{-1}) at 850 hPa at 0000 UTC 1 Jul 1991. In (a) the heavy dashed arrow and heavy dashed line indicate the southwesterly jet stream and wind shear line, respectively. In (b) the heavy dashed line indicates the anomalous convergence line. Letters "A" and "C" denote the anticyclone and cyclone centers. The straight dashed line is along 114.75°E longitude, which will be used for vertical–latitude cross-section plots in Fig. 4. (c) Total and (d) anomalous height and temperature at 925 hPa, where the heavy dashed line denotes trough height, contour for height (10-gpm interval) and color shading for temperature (1-K interval). Red, green, and blue open circles (dots) indicate the stations with rainfall over 50, 25–50, and 10–25 mm day^{-1}, respectively. Purple contours are the isohyets of 10, 25, and 50 mm day^{-1} using the interpolated gridded precipitation.

on an anomaly map. For example, Fig. 3 compares the horizontal view of conventional and anomaly weather maps for a heavy rain case (Qian et al. 2016b). The heavy rainband is, in a loose sense, located on the left side of a low-level jet (Fig. 3a) and the right side of a low-level geopotential height trough (Fig. 3c) on the full-field map. However, it is, in a more precise sense, collocated with a wind convergence zone (Fig. 3b), a geopotential height trough and a temperature front (i.e., the boundary between negative and positive temperature anomalies) (Fig. 3d) on the anomaly map. In other words, the heavy rainband and the anomaly features are better correlated in physical location on the anomaly map. The same is true for other weather phenomena.

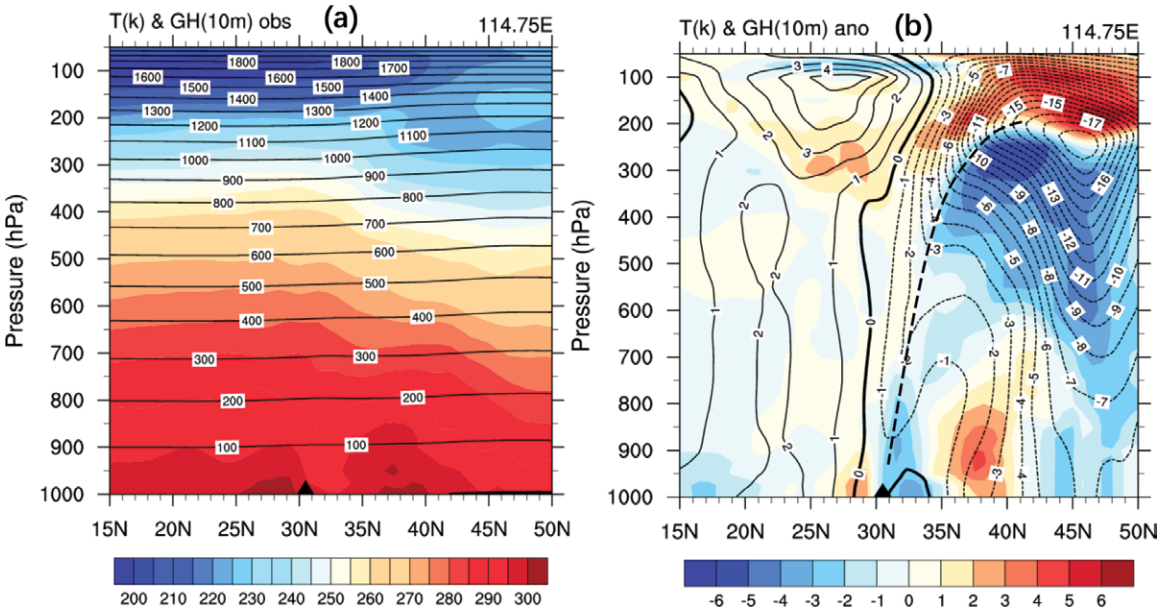

Fig. 4. Vertical pressure–latitude cross sections of (a) total and (b) anomalous height and temperature along 114.75°E longitude at 0000 UTC 1 Jul 1991. Contours are for height and color shading for temperature. The heavy dashed line denotes the axis of height anomalies in (b). The location of the surface rainband is indicated by the symbol ▲. The contour interval is 100 × 10 gpm for height and 5 K for temperature in (a), while it is 1 × 10 gpm and 1 K in (b).

Second, vertical structures of a weather system can be revealed more clearly and completely on an anomaly map. For example, Fig. 4 compares the vertical view of conventional and anomaly weather maps for the same heavy rain case. The heavy rainband is located at the lower end of the vertically extended anomalous trough and between the positive and negative temperature anomalies (Fig. 4b), while these features are not so strikingly visible on the conventional map (Fig. 4a). The anomaly map also reveals that the heavy rain event is associated with a well-organized structure that penetrates into the whole atmosphere, while the conventional map reveals little information on this deep structure with a mere near surface event. Similarly for the U.S. 2012 Hurricane Sandy case (Qian et al. 2016a), the entire vertical structures (such as low geopotential height and warm core temperature) of the hurricane itself and the surrounding weather systems are vividly seen on the anomaly map (Figs. 5b,d), while they are not as visible on the conventional map in both zonal and longitudinal directions (Figs. 5a,c). From Figs. 3–5, we can see that with the climate background removed, the anomaly features are directly associated with weather events of interest and show great spatial details of the disturbances.

Third, given enhanced disturbance signals, either the time or spatial evolution of an event or a series of events is much easier to observe on an anomaly map. Figure 6a shows a time sequence of anomalous temperature and geopotential height in Beijing over a winter month (December 2016). The eight upper-air abnormally warm periods (causing temperature inversions near the surface) were clearly observed, which exactly correspond to the eight air pollution episodes (Fig. 6b) (Qian and Huang 2019). The abnormality of the warm episode is also positively correlated to the severity and duration of the air pollution. However, these characteristics are not obviously visible in the conventional weather maps (not shown). By examining the spatial evolution of consecutive anomaly maps, the involved physical processes or interactions with surrounding weather systems can also be clearly observed. For example, Fig. 7 vividly shows the extratropical transition process of 2012 U.S. Hurricane Sandy when the hurricane made landfall and merged with an anomalous cold air mass from the northwest. This merging process with the cold cored anomalous low

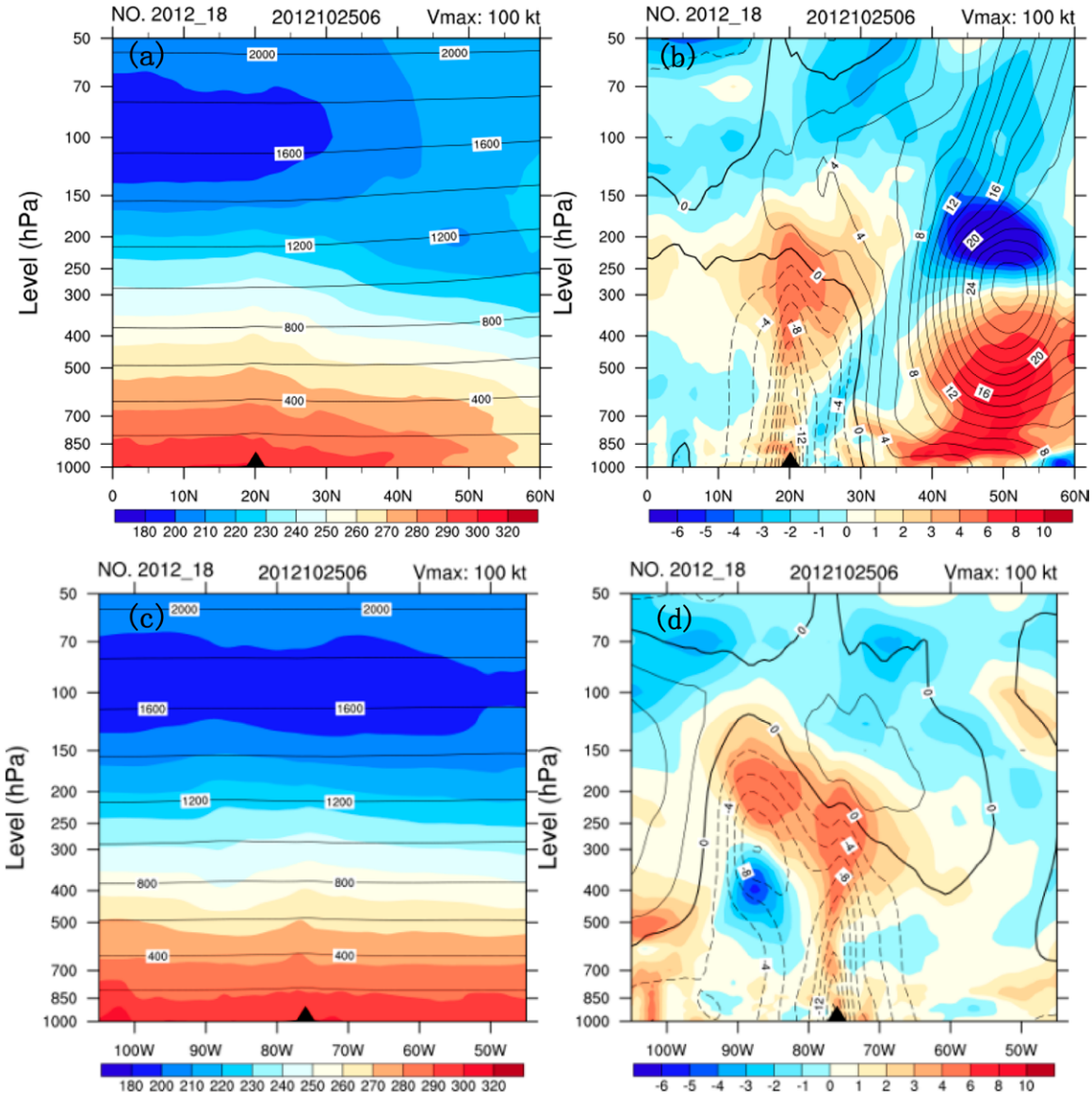

Fig. 5. Vertical pressure–longitude cross section of (a) total and (b) anomalous height and temperature along Hurricane Sandy's center at 0600 UTC 25 Oct 2012. Contours are for height [200 × 10-gpm interval in (a) and 2 × 10-gpm interval in (b)] and color shading for temperature [10- and 1–2-K intervals for (a) and (b), respectively]. The location of Sandy is indicated by the symbol ▲. (c),(d) As in (a) and (b), but for the vertical–latitude cross section along the hurricane center.

was also apparent in anomaly vertical cross-section charts (Qian et al. 2016a). For large-scale and distant meteorological connections (such as teleconnections), anomaly weather maps have obvious advantages over full-field weather maps. On anomaly weather maps one can clearly relate an anomalous event in one area to other anomalous weather systems in remote areas. For example, Du et al. (2013) showed (in their anomaly weather maps Figs. 11 and 12) that the heavy rain event over the Beijing region had a direct connection with a tropical cyclone in south China (transporting moisture) and a persistent anomalous blocking in northeast Asia (slowing down northeastward moving low pressure systems). This blocking system is a part of the slow-moving Rossby wave train in the high latitudes, with the alternating positive and negative anomalous height centers clearly visible on the anomaly map (their Fig. 12). Even though such distant connections might be deduced by an experienced meteorologist, it is qualitative on a conventional weather map. It is, however, quantitative for a forecaster to assess how abnormal a field is relative to normal situation (climate) on an anomaly map.

Fourth, the anomaly approach could simplify conceptual models by unifying different weather systems or even completely opposite weather phenomena into one category. Thus, different weather phenomena can be analyzed and predicted using the same unified method. For instance, on an anomaly weather map all kinds of low pressure systems (such as a southwest vortex, subtropical cyclone and tropical cyclone) all show as an anomalous low; air pollution and fog can be viewed as a similar temperature inversion pattern (the former is a dry inversion, and the latter is a wet inversion) (Qian and Huang 2019; Qian et al. 2019a); and heat waves and cold surges can be categorized into the same temperature-anomaly event (Qian et al. 2016e). Figure 8 is the composite vertical profiles (along longitude and latitude, respectively) of anomalous temperature and height from 378 cold surge events (the upper panel) and 164 heat wave events (the lower panel). For a cold surge, the typical pattern is "a negative center of height anomaly at the upper troposphere, a shallow positive center of height anomaly near the surface, a cold air column below the upper low center and a warm column above" (Qian et al. 2016e). The height anomalies and temperature anomalies are internally correlated with the hydrostatic balance. For a heat wave, the anomalous pattern is the same but with opposite signs. Qian et al. (2016e) showed that these anomalous height centers at the upper troposphere are correlated to the surface air temperature anomalies. When the upper-air warm (cold) anomaly reaches the ground, a heat wave (cold surge) event happens at the surface. Therefore, we can use the negative (positive) anomalous height center [named the maximum height anomaly (MHA)] at the upper troposphere to trace a cold surge (heat wave) event at the surface in a unified way.

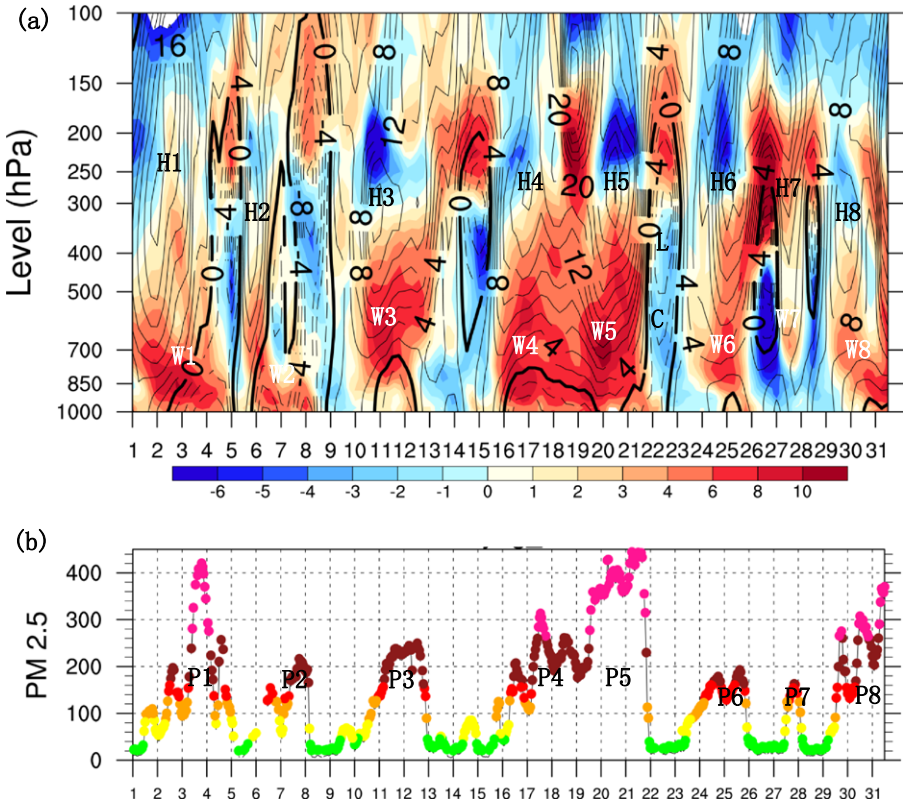

Fig. 6. (a) The vertical pressure–time cross section of height (2 × 10-gpm interval) and temperature (1- and 2-K intervals) anomalies at Beijing from 1 to 31 Dec 2016. (b) The time variation of $PM_{2.5}$ concentration ($\mu g\ m^{-3}$) at Beijing over the same time period. Legend: H = positive height anomaly center; W = warm temperature anomaly; and P = peak of $PM_{2.5}$ concentration. There were eight air pollution episodes that occurred.

Finally, given the much clearer and amplified disturbance signals on anomaly weather maps, one would expect that meaningful warning signals or predictors could possibly be seen earlier if NWP model forecasts are displayed in the form of anomaly maps. In other words, model forecast length could possibly be extended by using anomaly maps instead of traditional maps. For example, as discussed in the last paragraph (Fig. 8), the signal of the anomalous height center in the upper troposphere (i.e., MHA) is much stronger than that of the surface temperature anomaly. Therefore, the forecasts of heat waves or cold surges can be greatly extended if we trace MHA instead of surface temperature anomalies. Our result shows that positive or negative MHA centers can be traced, on average, nine days ahead for

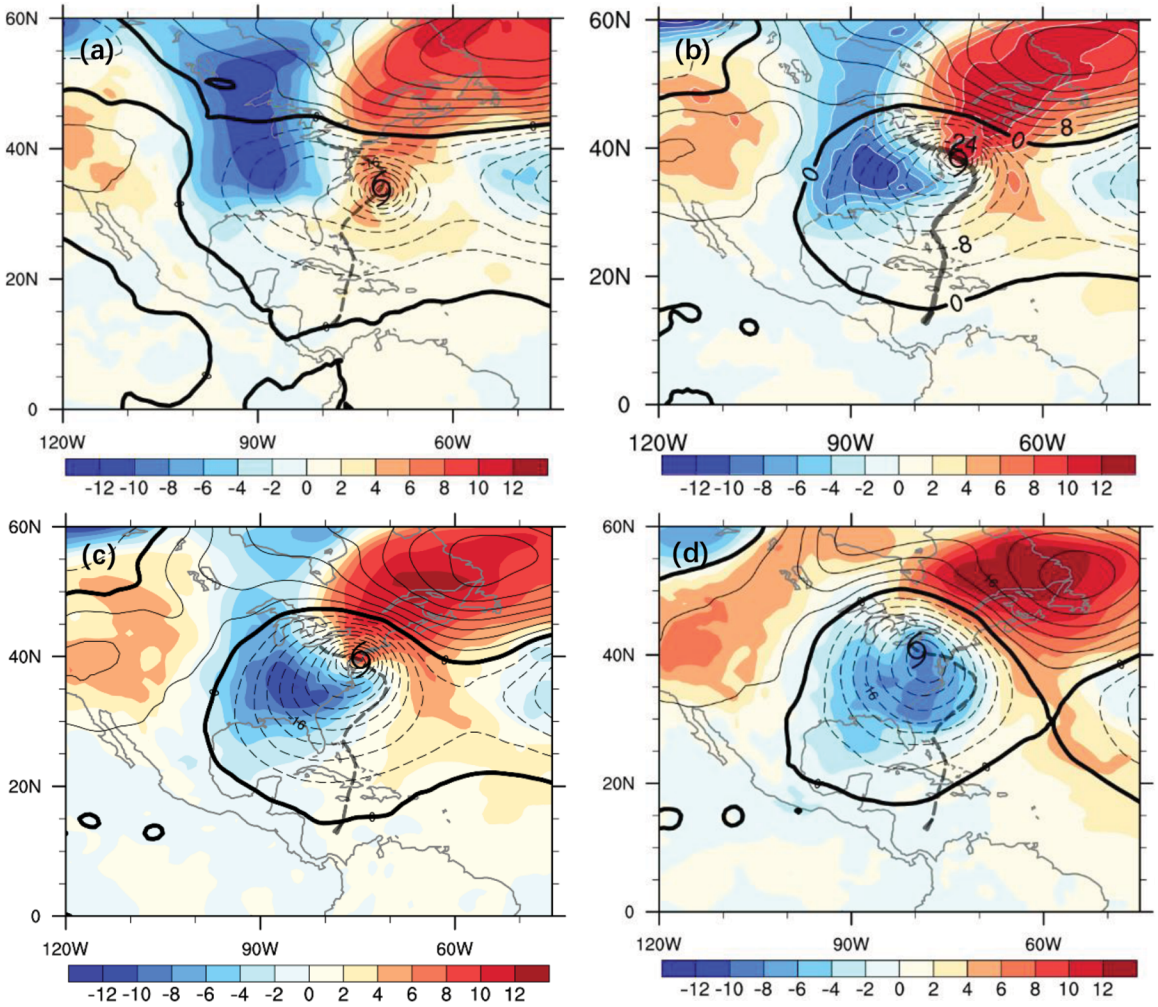

Fig. 7. Time evolution of height anomaly (positive is solid and negative is dashed; 4 × 10-gpm interval) and temperature anomaly (shading; 2-K interval) at the 700-hPa level for (a) 0000 UTC 29 Oct, (b) 1800 UTC 29 Oct, (c) 0000 UTC 30 Oct, and (d) 0000 UTC 31 Oct 2012.

surface air temperature anomaly events (heat waves and cold surges) in ECMWF global model forecasts. Figure 9 shows three heat wave cases, where the MHA signal indicates a heat wave event can be steadily traced 20–26 days back to an upstream region in the ECMWF model forecast (Chen et al. 2017; Qian et al. 2016d,e; Qian and Jiang 2014). A similar forecast length extension was also seen in the air pollution case by using an anomaly map similar to Fig. 6. Such anomalous patterns ("fingerprints") of major weather events can be detected by using an artificial intelligence technique such as pattern recognition to increase the utility of an NWP model prediction, as demonstrated by the work of Grumm et al. (2005) and Root et al. (2007).

In addition to the above five advantages, an anomaly map can be used to evaluate forecasts. For example, Fig. 10 is the altitude–forecast hour (7.5-day forecast) cross section of a hurricane center's anomalous height and temperature, predicted by two global models (ECMWF and NCEP GFS) initialized at 0000 UTC 24 October 2012 for Hurricane Sandy (Qian et al. 2016a). It clearly shows the differences in performance between these two models. By comparing to the analyzed anomalous fields (Fig. 10c), two major differences are clearly visible: 1) the extratropical transition (ET) process from 30 to 31 October was correctly captured by the ECMWF model but missed by the NCEP GFS, because the GFS failed to predict Sandy's left-turning landfall when it moved northward; and 2) the ECMWF model predicted the hurricane center pressure as too low, while the GFS forecast is closer to the analysis. Whether or not the anomaly-based verification method has a systematic advantage over the full-field-based verification method needs to be further

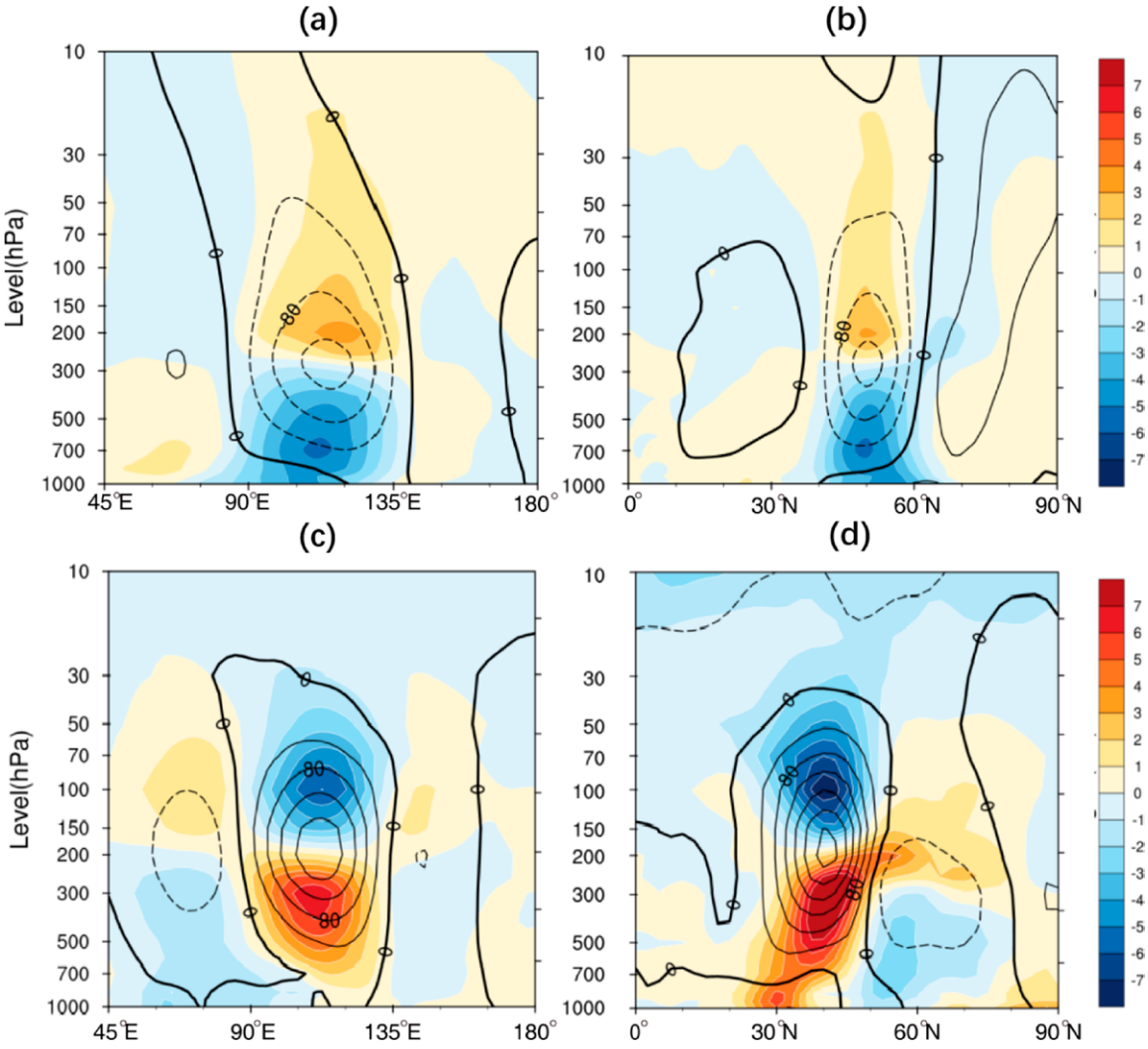

Fig. 8. The 378-day cold-surge case composites of height (40-gpm interval) and temperature (1-K interval) anomalies for two vertical cross sections along (a) 50°N latitude and (b) 112.5°E longitude. The 164-day heat-wave case composites of height and temperature anomalies for two vertical cross sections along (c) 40°N latitude and (d) 112.5°E longitude.

investigated. Van den Dool (2007) did show that the anomaly correlation better reflects the true quality of a forecast than a full-field-based correction in climate study. The anomaly correlation is now a standard measure to verify an NWP weather forecast at NCEP (J. Du 2020, personal communication).

Anomaly forecast. In seasonal and short-term climate forecasting, qualitative anomaly (e.g., above, at or below a normal climatic state) is a commonly used format due to the lack of predictability in detailed atmospheric motions (Van den Dool 2007). During the last two decades

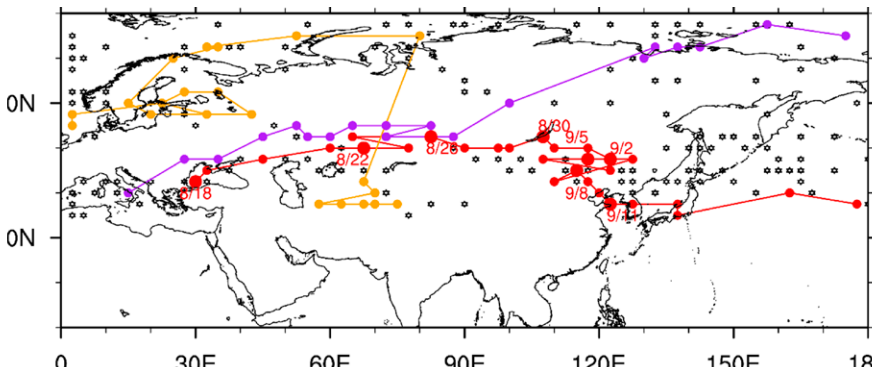

Fig. 9. Daily points of maximum height-anomaly (MHA) centers during the two months of August and September in 1999. Three colored lines show the tracks of three MHA centers. Dates were also marked for the red line, e.g., "8/18" and 8/22" indicate the dates of 18 Aug and 22 Aug 1999.

a quantitative anomaly forecast has also been introduced to short-range weather forecasts, especially for high-impact weather events (Grumm and Hart 2001; Hart and Grumm 2001; Junker et al. 2008, 2009; Graham and Grumm 2010; Grumm 2011a,b; Du et al. 2013; Alcott et al. 2014; Lamberson et al. 2015). This quantitative anomaly forecast (hereafter referred to as "anomaly forecast") has been widely accepted by the weather forecasting community since it is useful in raising a user's awareness of potential societal impact.

Unlike anomaly weather maps where the absolute anomaly [Eq. (2)] is used, anomaly forecasts use the standardized anomaly [SA; Eq. (3)]. This is because climate varies greatly with location and time, only SA can truly reflect the local significance of a weather forecast in terms of how unusual a forecast is relative to its climatic variation. The SA is an anomaly normalized by the standard deviation of climate variation:

$$\mathrm{SA}_{(d,y)}(\lambda,\varphi,p,t)=\frac{\upsilon_{(d,y)}(\lambda,\varphi,p,t)-\tilde{\upsilon}(\lambda,\varphi,p,t)}{\sigma_{\mathrm{clim}}(\lambda,\varphi,p,t)}, \qquad (3)$$

where $\sigma_{\mathrm{clim}}(\lambda, \varphi, p, t)$ is the standard deviation of climatic variation of a variable, and the rest are the same as in Eq. (2). When $\upsilon_{(d,y)}(\lambda, \varphi, p, t)$ is a forecast, $\mathrm{SA}_{(d,y)}(\lambda, \varphi, p, t)$ becomes an anomaly forecast. Jiang et al. (2016) has a comparison study between the two forms of anomalies: the absolute anomaly from Eq. (2) and the normalized anomaly relative to climatic variation from Eq. (3).

Initially, the SA was used to assess the rareness of an event in history by comparing it with the climatological variation (Grumm and Hart 2001; Hart and Grumm 2001; Junker et al. 2008, 2009; Graham and Grumm 2010; Grumm 2011a,b). Later on SA was further combined with ensemble forecasts to not only assess its rareness but also to estimate the likelihood of its occurrence as well as its potential societal impact (Du et al. 2013; Alcott et al. 2014; Lamberson et al. 2015). Du et al. (2013) will be used below as an example to demonstrate these three aspects.

Figures 11a–c are the anomaly forecasts (in color) derived from the single deterministic GFS model outputs, based on Eq. (3) for a heavy rain event (Du et al. 2013). We can see that the SA of both 850-hPa southerly wind υ (Fig. 11a)

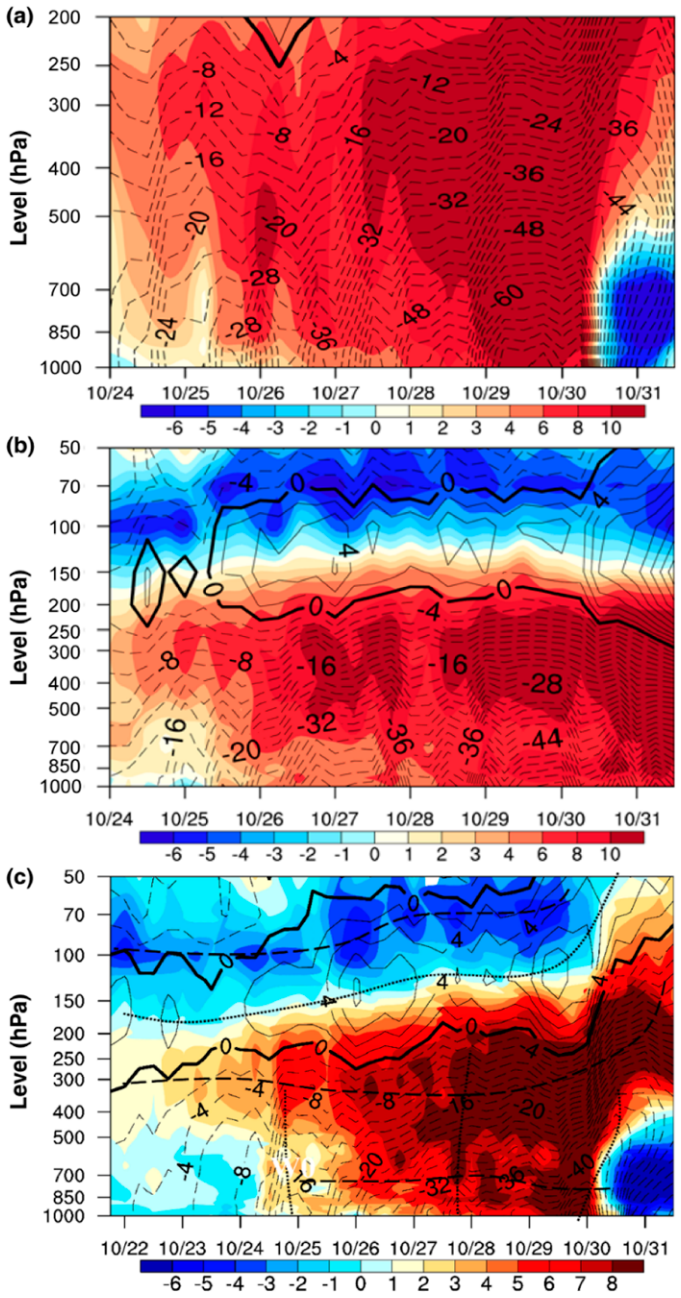

Fig. 10. Vertical pressure–time cross sections of height anomalies (positive in a solid line and negative in a dashed line; 2 × 10-gpm interval) and temperature anomalies (shading; 1-K interval) with 6-h interval for (a) ECMWF model forecast (0000 UTC 24 Oct–1200 UTC 31 Oct), (b) NCEP GFS forecast (0000 UTC 24 Oct–1200 UTC 31 Oct), and (c) ERA-Interim analysis (1800 UTC 21 Oct–1200 UTC 31 Oct 2012). In (c), the heavy dotted line and the heavy dashed line are the axes of height anomalies and temperature anomalies, respectively. Three vertical axes of height anomalies at the mid–low troposphere are indicated by the heavy dotted line at 1800 UTC 24 Oct, 1800 UTC 27 Oct, and 0000 UTC 30 Oct, respectively.

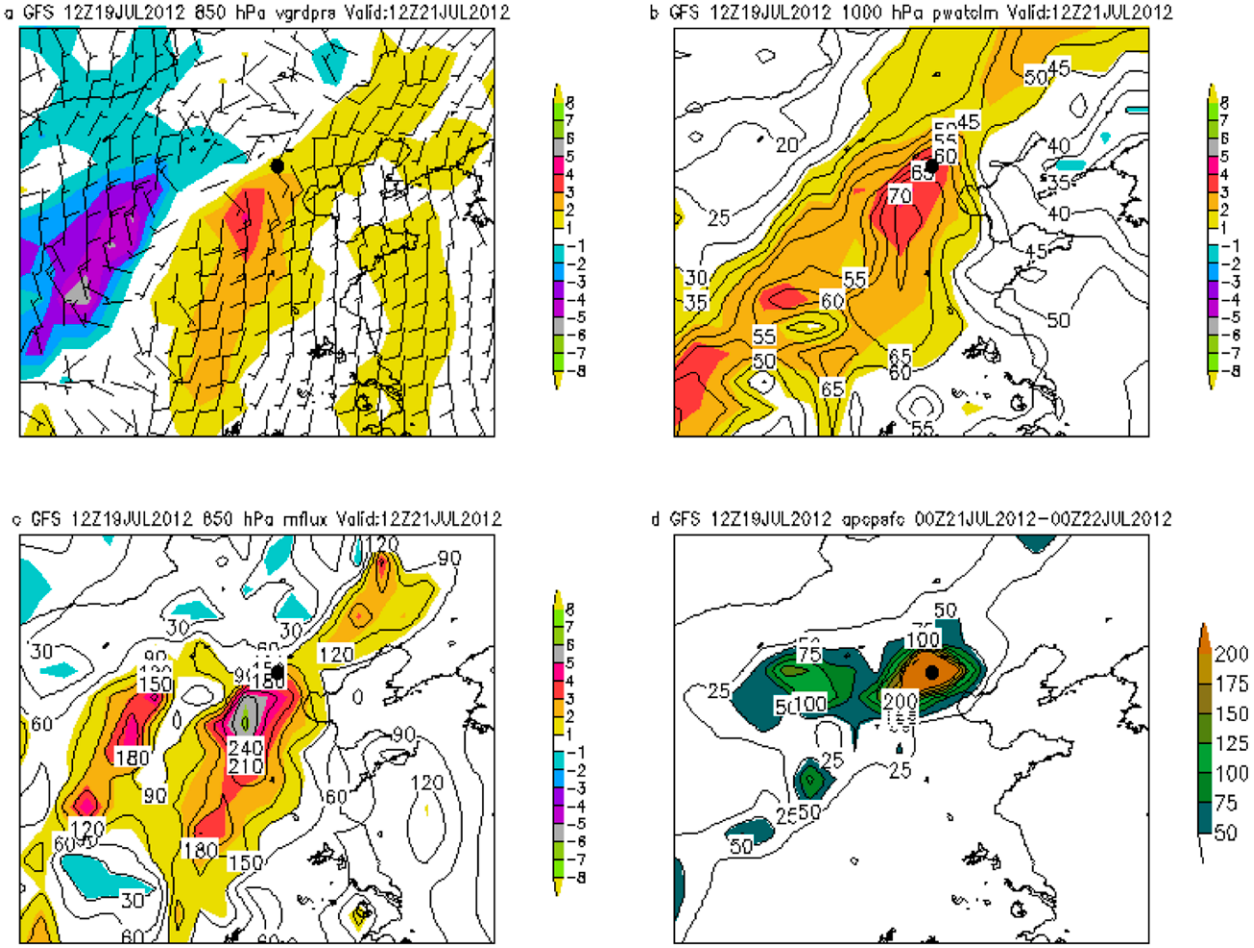

Fig. 11. The NCEP 27-km single GFS 48-h forecasts of (a) 850-hPa winds (vectors; m s^{-1}) and southerly wind *v* anomalies SA (color; 1-SD interval), (b) precipitable water (contours; 5-mm interval) and its anomalies SA (color, 1-SD interval), and (c) 850-hPa horizontal moisture flux (contours; 30 × 0.01 g kg^{-1} × m s^{-1} interval) and its anomalies SA (color; 1-SD interval), initiated at 1200 UTC 19 Jul and valid at 1200 UTC 21 Jul 2012. (d) The GFS 60-h forecast of accumulated quantitative precipitation (25-mm interval) for the 24-h period of 0000–2400 UTC 21 Jul, initiated at 1200 UTC 19 Jul and valid at 2400 UTC 21 or 0000 UTC 22 Jul 2012. The black dot is Beijing.

and precipitable water (Fig. 11b) exceeded three standard deviations (SD) of climate variance, and the SA of the 850-hPa horizontal moisture flux (Fig. 11c) was even stronger and exceeded six standard deviations, suggesting a potentially very significant heavy rain event would occur in its immediate downstream region. This high SA information would certainly give forecasters a high confidence about the significance level of the upcoming heavy rain as predicted by Fig. 11d.

Although the anomaly forecast derived from a single forecast (as in Fig. 11) can provide forecasters information about the significance level of a potential weather event, it does not provide quantitative information about the confidence level of the forecast itself (i.e., likelihood of occurrence). If we combine an anomaly forecast together with ensemble forecasts (Du et al. 2018), then both the significance level of an upcoming event and the confidence level of the forecast can be obtained at the same time. For example, when Eq. (3) was applied to each member of the GEFS ensemble, a probabilistic forecast of SA exceeding a fixed threshold can be calculated. Figure 12 is the probabilistic forecasts (in color) of SA exceeding three standard deviations for three variables. The probability of SA exceeding three standard deviations is over 80% for the southerly wind *v*, and 100% for both precipitable water and horizontal moisture flux, suggesting the upcoming event is not only significant but also highly

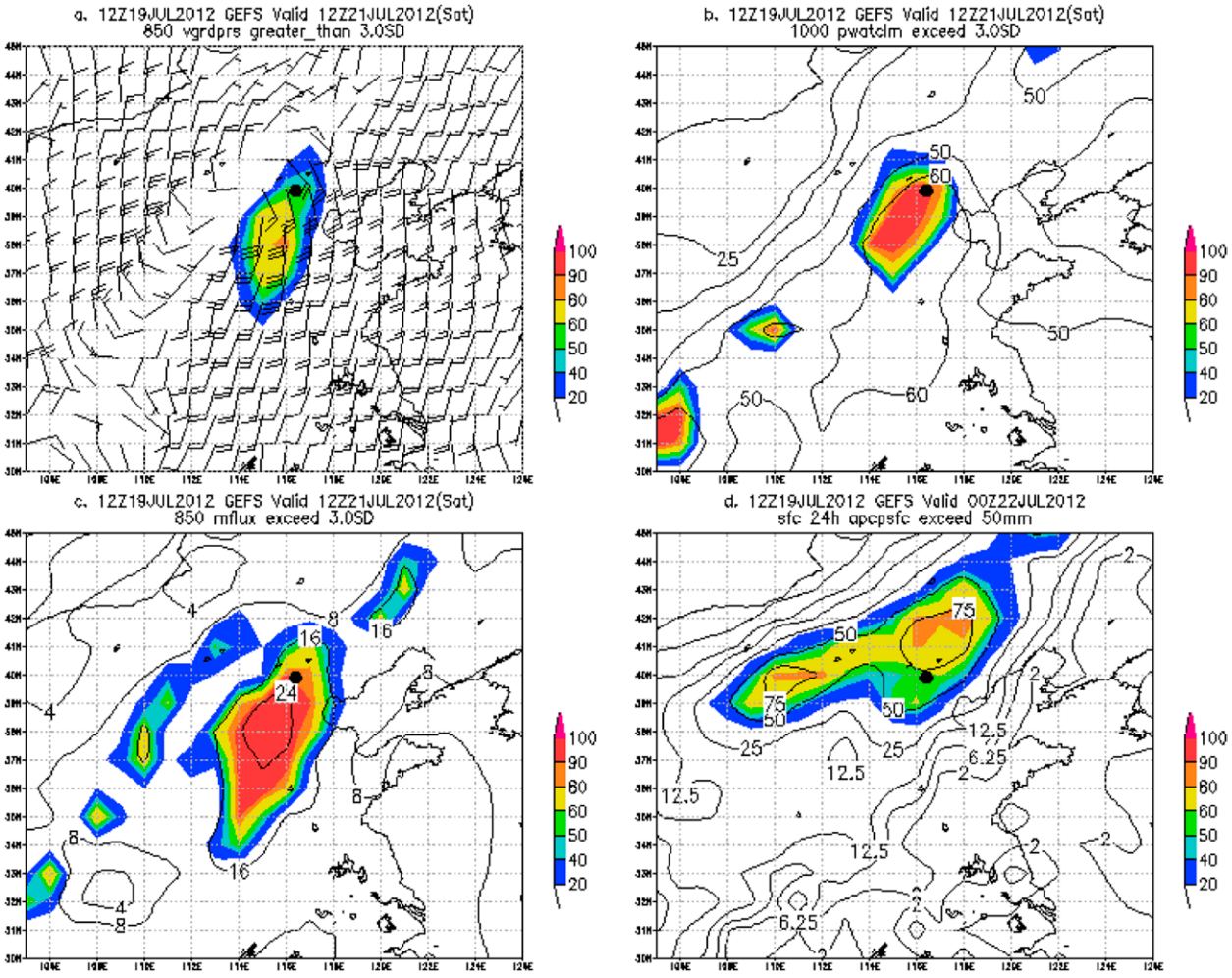

Fig. 12. The NCEP 55-km GEFS 48-h forecasts of (a) 850-hPa ensemble mean winds (vectors; m s^{-1}) and the probability (%) that the SA of southerly wind v exceeds three standard deviations (color), (b) ensemble mean precipitable water (contours; mm) and the probability (%) that its SA exceeds three standard deviations (color), and (c) 850-hPa ensemble mean moisture flux (contours; 0.01 × g kg^{-1} × m s^{-1}) and the probability (%) that its SA exceeds three standard deviations (color), initiated at 1200 19 Jul and valid at 1200 21 Jul 2012. (d) The GEFS 60-h forecast of ensemble mean accumulated quantitative precipitation (mm) and the probability (%) that the rainfall exceeds 50 mm for the 24-h period of 0000–2400 UTC 21 Jul, initiated at 1200 UTC 19 Jul and valid at 2400 UTC 21 or 0000 UTC 22 Jul 2012. The black dot is Beijing.

likely to occur. Figure 12d shows the 60-h forecasts of ensemble mean and the probability of exceeding 50 mm for 24-h accumulated rainfall.

Further, when information like Figs. 11 and 12 is combined together, a societal impact matrix can be defined (Du et al. 2013; Suri 2015; Economou et al. 2016; Bevan 2017). How to form this matrix? Different people had different ways. The Met Office has done some extensive work on this aspect (Suri 2015; Economou et al. 2016; Bevan 2017). The western regional office of the National Weather Service (NWS) has been experimenting with it in operations too (Alcott et al. 2014; Lamberson et al. 2015). In Du et al. (2013) the significance level (a function of SA) is as the x axis, forecast confidence (a function of probability) as the y axis, and the multiplication of x and y is the value of matrix elements or the societal impact index (SII) (Fig. 13). Apparently, a predicted event with higher SA and higher probability (yielding a higher SII) will be both more significant relative to climate and more likely to occur, implying a higher societal impact. Therefore, SII is an indicator of the situational awareness level of a forecast, either giving heads up or down to forecasters and users. How to construct an optimal societal impact matrix could be user or situation dependent. In Fig. 13, the x axis uses

2 × SA as the interval, while the *y* axis uses 1/10 of probability (in %) as the interval, where SA refers to the ensemble mean forecast and the probability is calculated from all ensemble members exceeding this SA value. For example, if the SA = 4 in the ensemble mean and the probability of SA exceeding 4 is 90%, it gives the SII a value of 72, indicating a high impact event to society. Since an SII can be calculated at each individual location or a grid point, SII can be displayed either at a point or on a two-dimensional map for forecaster use. For an ensemble prediction system and a type of weather event, a large number of cases are needed to find out the average value of SII, so that it will give a forecaster or a user a quantitative threshold to distinguish between a higher or lower societal impact event. These representative SII values could be pre-estimated by using ensemble reforecasting dataset (Hamill et al. 2013). Physical understanding of the relationship between an SII value and a real world application is also needed.

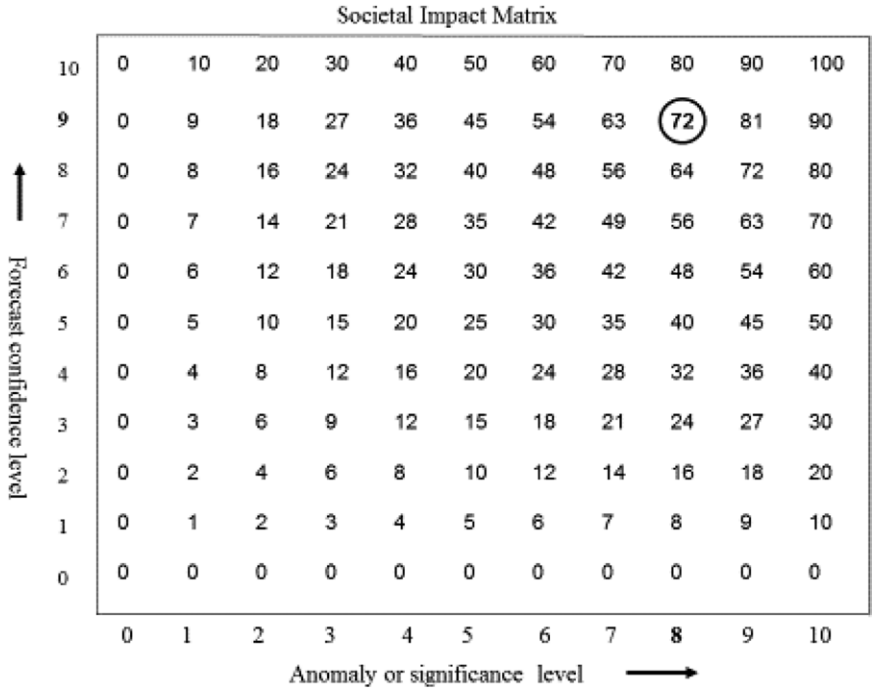

Fig. 13. "Societal impact matrix" of a weather forecast: the horizontal axis indicates the anomalous (significant) level of a predicted weather event, the vertical axis the confidence level of the forecast. A higher matrix-element value [defined as "societal impact index" (SII)] indicates higher societal impact potentially caused by the predicted weather event.

Note that SII is calculated from an individual variable, but there may be several variables key to a real world event such as heavy rain in this case (e.g., 850-hPa *υ*, precipitable water, and 850-hPa moisture flux, Figs. 11 and 12). Which variable's SII should be used as the final indicator for this heavy rain event? The answer could depend on a forecaster's scientific insight and experience: it could be a single SII of the most significant variable like the 850-hPa moisture flux, or a weighted/unweighted average or a certain combination of the three SIIs from all variables. The NWS western regional office has developed a real-time monitoring website with a situational awareness table for eight selected variables based on the North American Ensemble Forecast System's global ensembles (https://satable.ncep.noaa.gov/naefs and http://ssd.wrh.noaa.gov/satable). These efforts are very helpful to deepen our understanding of this SII work and guide us to wisely select meaningful variables. For instance, their table shows a quite promising signal: different types of weather events may share similar significant variables.

Diagnostic parameters. Anomaly fields are not only more clear in depicting weather disturbances through anomaly weather maps but are also more indicative in constructing diagnostic parameters for a weather event. Two examples will be demonstrated in this subsection. Figure 14 shows the vertical distributions of the total (Fig. 14a) versus anomalous (Fig. 14b) heights and temperatures along 34°N at 0600 UTC 28 April 2011 for a tornadic event. Similar to what we have already seen above, the vertical structure is much more striking in the anomaly field than the full field. Convective instability indices derived from the total temperature and anomalous temperature are shown in Figs. 14c and 14d, respectively. Figure 14c is the traditional lifted index (LI) which is defined as the temperature

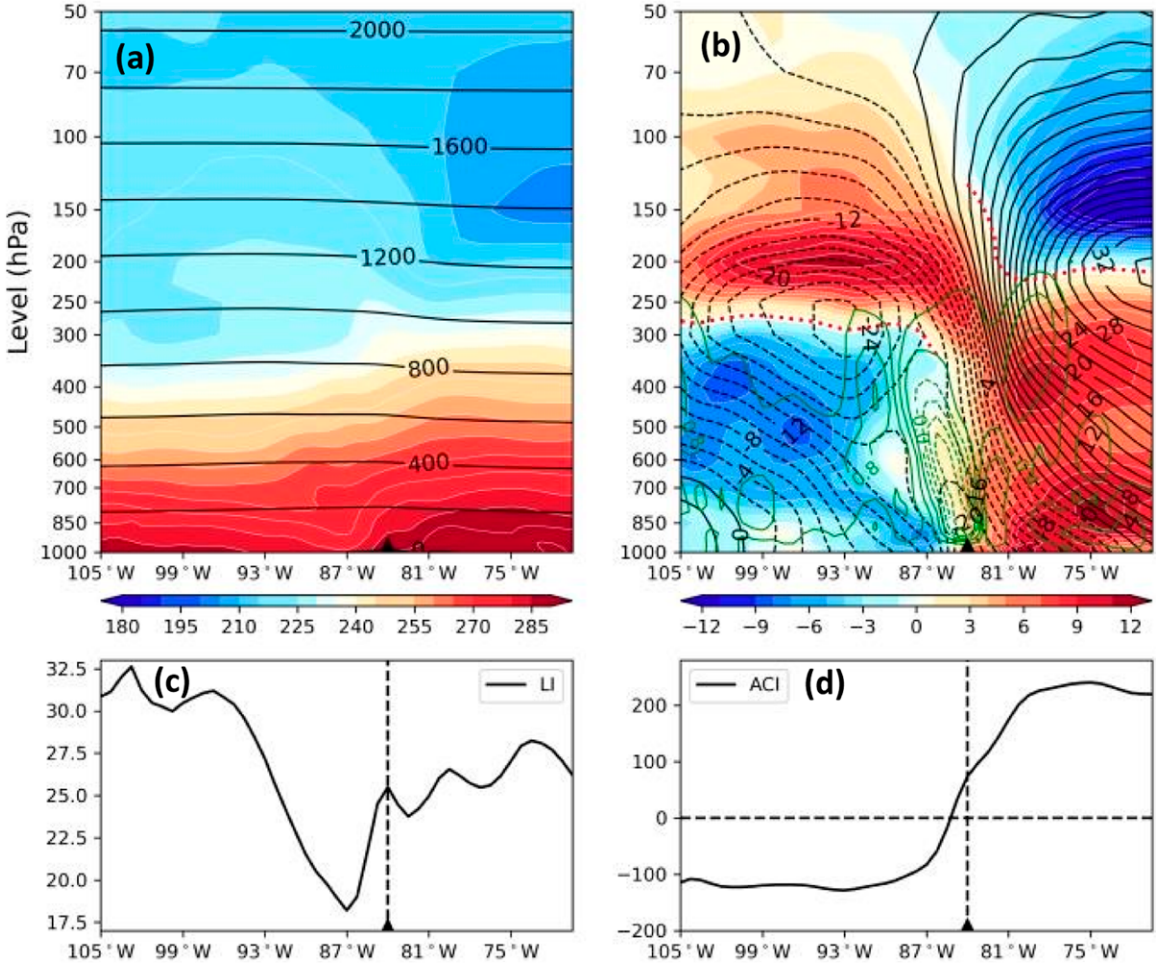

Fig. 14. Vertical pressure–latitude cross sections of (a) total height (contours; 200 × 10-gpm interval) and temperature (shading; 15-K interval), and (b) anomaly height (contours; 2 × 10- gpm interval) and temperature (color; 3-K interval) along 34°N at 0600 UTC 28 Apr 2011. (c) The traditional lifted index (LI) and (d) the anomalous convective instability (ACI) index. The triangle "▲" indicates the central position of the surface anomalous low associated with the tornadic storm. The green solid and dashed lines, respectively, indicate anomalous sinking and rising pressure velocities (0.2 Pa s^{-1} interval). The red-dotted line vertically separates the anomalous warm air mass from the anomalous cold air mass in (b). Heavy rainfall and tornedoes occurred near the triangle on the anomalously warm and rising flow side.

difference between the 500- and 850-hPa levels. Figure 14d is the anomalous convective instability (ACI) index, which is defined in Qian et al. (2019b) as the difference of vertically integrated temperature anomalies T' between two opposite anomalous air masses from 1,000 to 100 hPa [Eq. (4)]:

$$\mathrm{ACI} = \left[\int T' dp\right]_{\text{lower-layer}} - \left[\int T' dp\right]_{\text{upper-layer}}. \tag{4}$$

The boundary of the two opposite anomalous air masses [marked as "upper-layer" and "lower-layer" in Eq. (4)] is defined by the zero temperature anomaly (Fig. 14b). For the lifted index, the tornado event is associated with one of many LI peaks (Fig. 14c). For the anomalous convective instability, the tornado occurred near the sole zero line of ACI on the positive side (Fig. 14d). The signal of ACI is much more distinct than that of LI because the difference between the positive and negative values in the ACI is vastly larger and steadier due to the integration of anomalous information from the entire atmosphere. The ACI is also capable of distinguishing the severity of convective storms. For example, the value of ACI for 15 tornadic

storms is, on average, 1.5 times larger than that for 20 hailstorms (Qian et al. 2019b). Their results showed that the ACI index also outperformed other full-field-based indices, including convective available potential energy (CAPE), updraft helicity (UH), and severe weather threat (SWEAT) in detecting tornadic and hailstorms.

Qian et al. (2015) systematically compared the full-field version with various anomaly field versions of seven parameters for diagnosing heavy rain areas. The seven parameters are vorticity (Vort), divergence (Div), moist vorticity [MV; Eq. (5)], moist divergence [MD; Eq. (6)], specific humidity (*Q or q*), Q vorticity [VQ; Eq. (7)], and Q divergence [DQ; Eq. (8)] for diagnosing heavy rain areas (Qian et al. 2015, 2016c):

$$\mathrm{MV} = \left(\frac{\partial v}{\partial x} - \frac{\partial u}{\partial y}\right) \times \left(\frac{q}{q_s}\right)^{10}, \tag{5}$$

$$\mathrm{MD} = \left(\frac{\partial u}{\partial x} + \frac{\partial v}{\partial y}\right) \times \left(\frac{q}{q_s}\right)^{10}, \tag{6}$$

$$\mathrm{VQ} = \left(\frac{\partial v}{\partial x} - \frac{\partial u}{\partial y}\right) \times q, \tag{7}$$

$$\mathrm{DQ} = \left(\frac{\partial u}{\partial x} + \frac{\partial v}{\partial y}\right) \times q, \tag{8}$$

where q/q_s is the ratio of specific humidity to saturated specific humidity (i.e., relative humidity). After evaluating 41 heavy rain cases occurring in 1998, their results showed that except for divergence and MD, the anomaly-based version outperformed the corresponding full-field-based version for the other five parameters (Fig. 15). The results also showed that for multivariable parameters, a hybrid version (i.e., anomaly for one variable and full field for another) often performed better than a pure-anomaly version (i.e., anomaly for all variables).

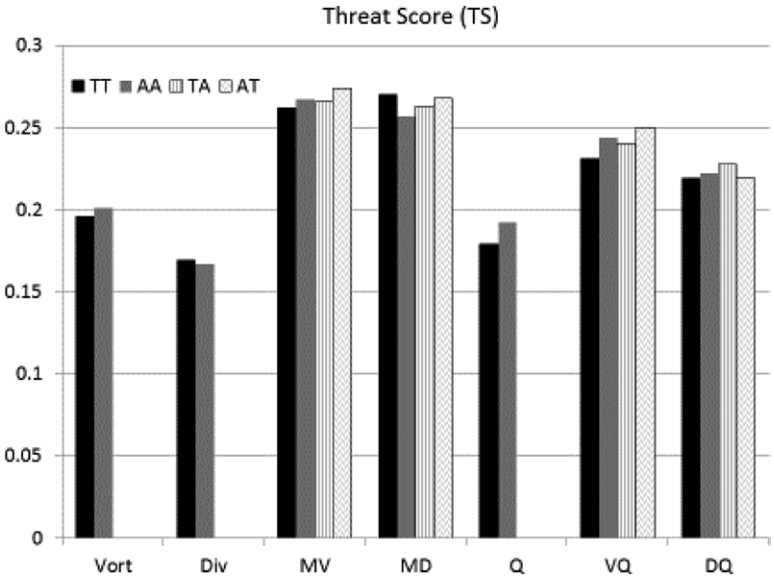

Fig. 15. Average threat scores (TSs) of the seven parameters (Vort = vorticity; Div = divergence; MV = moist vorticity; MD = moist divergence; Q = specific humidity; VQ = vorticity × specific humidity; and DQ = divergence × specific humidity) in depicting heavy precipitation area (≥25 mm day^{-1}) based on a total of 41 daily heavy rain cases that occurred in eastern China during 1998. Legend for different versions: TT = all total field(s); AA = all anomalous field(s); TA = total wind field × anomalous moisture field; and AT = anomalous wind field × total moisture field.

Model prediction. The anomaly approach has also been applied to the prediction model itself. For example, NOAA/GFDL and Princeton University have experimented with an anomaly GCM for long-range weather forecasts (Miyakoda and Chao 1982). They argued that "there may be a limitation on the pure GCM forecasts for the seasonal range. An anomaly model may provide a remedy as the accurate and economical forecasting method." Guo and Chao (1984) further developed this anomaly model into a filtered

anomaly model or anomalous filtered model (AFM), in which transient Rossby waves are filtered. Chao et al. (1986) applied a version of the three-layer AFM to monthly predictions of eight winter months during the 1976/77 and 1982/83 El Niño periods. They showed that the AFM can successfully predict the large-scale patterns of the monthly mean surface temperature anomalies and outperformed persistence forecasts.

Since a state of the art NWP model is highly nonlinear, complex and interactive at all scales and physics, it is extremely challenging, if not impossible, to decompose it into climate and anomaly components. Therefore, a simple dynamical model is used in Qian et al. (2014) and Huang et al. (2015) to build an anomaly model for short-range forecasts of typhoon or hurricane track, which is used as a demonstration below. The barotropic vorticity equation thought to approximately govern the horizontal flow is written as follows:

$$\frac{\partial \zeta}{\partial t} = -u\frac{\partial \zeta}{\partial x} - v\frac{\partial \zeta}{\partial y} - \beta v + F, \tag{9}$$

where $\zeta = (\partial v/\partial x) - (\partial u/\partial y)$, $\beta = (df/dy) = 2\Omega\cos(\varphi/a)$, $f = 2\Omega\sin\varphi$, and $\Omega = 7.292 \times 10^{-5}$ rad s^{-1} is the angular speed of Earth's rotation. The terms a and φ are the mean radius of Earth and geographical latitude, respectively. The variable F is a generic forcing term that includes forces at all scales and dissipation such as divergence, friction, and diabatic processes. For nondivergent, frictionless and adiabatic atmospheric motion, $F = 0$. Equation (9) can be simplified as

$$\frac{\partial \zeta}{\partial t} = -u\frac{\partial \zeta}{\partial x} - v\frac{\partial \zeta}{\partial y} - \beta v. \tag{10}$$

Equation (10) indicates that the movement of a vortex such as a tropical cyclone is primarily controlled by the advection of relative vorticity and the Earth rotation beta effect. This is the classical total-flow-based two-dimensional beta-advection model (BAM). Depending on the steering flow layer used, there are three versions of BAM: BAM-Shallow (BAMS) applied to the 850–700-hPa layer, the BAM-Medium (BAMM) applied to the 850–400-hPa layer, and the BAM-Deep (BAMD) applied to the 850–200-hPa layer.

If the total flow is decomposed into climatic and anomalous flows [Eq. (2)], the BAM can be simplified into a so-called generalized beta-advection model (GBAM) (Qian et al. 2014; Huang et al. 2015):

$$\frac{\partial \zeta'}{\partial t} = -u\frac{\partial \zeta'}{\partial x} - v\frac{\partial \zeta'}{\partial y} - \beta v'. \tag{11}$$

The GBAM indicates that the vortex itself and beta effect can be described by anomaly flow alone but the steering flow needs to consider both climate and anomaly $[-u'(\partial\varsigma'/\partial x) - v'(\partial\varsigma'/\partial y), -\tilde{v}(\partial\varsigma'/\partial x) - \tilde{v}(\partial\varsigma'/\partial y)]$. Since the climatic flow is known, the prediction of a vortex can then be made based purely on anomalous flow.

Huang et al. (2015) systematically compared the performances of the total-flow-based BAM and

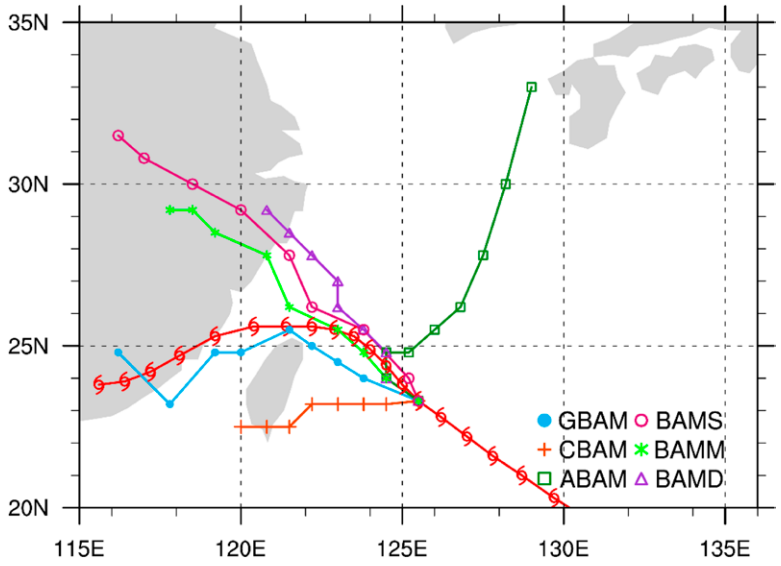

Fig. 16. The 48-h track forecasts of Typhoon Aere, initiated at 0600 UTC 23 Aug 2004 (24 h before the left turning), by six models—GBAM (blue solid dots) and the three versions of BAM: BAMS (pink open circles), BAMM (dark green asterisks), and BAMD (purple triangles), as well as CBAM (orange pluses) and ABAM (light green squares). The hurricane symbol indicates the best track.

anomalous-flow-based GBAM in predicting typhoon tracks (1–2 days in advance) using 133 tropical cyclones (TCs) occurring in the eastern China seas in 1979–2011. They found that the GBAM steadily outperformed the BAMs for both normal and unusual tracks. One example is given in Fig. 16, where the GBAM track successfully predicted the left turn of Typhoon Aere before it approached the mainland to make its landfall, while all three BAM versions (BAMS, BAMM, and BAMD) failed to predict this critical left turn but kept the track straight. This is true for the other TCs, in which the GBAM was particularly good in predicting unusual TC tracks but the BAM had no ability to predict left-turning and right-turning TC tracks. The stated reason for the superiority of GBAM to BAM lies in two factors: 1) The GBAM focuses on the main factors (e.g., separating the vortex from the steering flow) and 2) The steering flow level for the GBAM can be precisely estimated from anomalous vorticity or divergence at model initialization time. This is the level with the maximum vorticity anomaly (Max-VA) and minimum divergence anomaly (Min-DA). By the way, since the Max-VA or Min-DA level varies with the intensity of a TC, this pre-estimate of steering flow level at the model initialization time prevents the GBAM from extending its forecast length beyond 1–3 days, especially for rapid intensifying or decaying TCs.

Besides the better performance of the anomaly-based over the total-flow-based model, the anomaly-based model has another advantage in understanding physical processes, because it can easily isolate different components. For example, Huang et al. (2015) demonstrated that the GBAM can be used to understand unusual TC tracks by separating it into two forms: a climatic-flow BAM (CBAM),

$$\frac{\partial \zeta'}{\partial t} = -\tilde{u}\frac{\partial \zeta'}{\partial x} - \tilde{v}\frac{\partial \zeta'}{\partial y} - \beta v', \tag{12}$$

and an anomalous-flow BAM (ABAM),

$$\frac{\partial \zeta'}{\partial t} = -u'\frac{\partial \zeta'}{\partial x} - v'\frac{\partial \zeta'}{\partial y} - \beta v'. \tag{13}$$

The CBAM can test the steering impact of climatic flow, while the ABAM can test the anomaly flow impact. They found that neither the climatic or anomalous flow alone as the steering flow can explain unusual tracks (e.g., both CBAM and ABAM yielded unrealistic tracks compared to the best track, Fig. 16). The GBAM can easily be used to test the interaction of a TC with surrounding vortices. For example, by removing the surrounding anomaly vortex, their sensitivity experiments showed that two anomalous highs as well as a nearby TC played major roles in the unusual left turn of Typhoon Aere (2004).

Caveats of the anomaly approach. Anomaly maps and forecasts ["Anomaly weather map (charts)" and "Anomaly forecast" sections] are apparently more useful for more significant and larger-scale events that tend to affect large population centers. Due to the limitation in spatial and temporal resolution of available data, especially climatology, sometimes local and mesoscale weather can fall through the cracks in an anomaly-based system. An example (provided by one of the anonymous reviewers) is that dry air with light winds could cause local radiational cooling which could produce frost and damage crops. These conditions in the transition seasons could produce fog and stop aircraft. They tend to be very local or regional in scale and could possibly be missed by anomaly-based tools.

For the following two reasons, anomaly maps should not be used alone but together with full field maps. The first reason is regarding appearance. As discussed in Qian et al. (2016b), the physical interpretation of an anomaly weather map ["Anomaly weather map (charts)" section] needs to be done with caution because an anomaly field is only relative to climate and cannot show the full picture. For example, a high pressure system could appear as an anomalous low pressure system in an anomaly weather map if the total field is below the

climatic value. Similarly for wind, an anomalous southerly wind does not necessarily represent a true southerly wind in a full field weather map. At the same time, an anomaly map can help us to formulate a scientific question differently. One might ask "Why is there a high pressure system over there?" when looking at a full-field weather map, while the question could become "Why has a normally strong high pressure system become weaker?" when looking at an anomaly map. The second reason is regarding development. The development and evolution of an atmospheric system depends on actual weather systems. One cannot infer physical development based solely on anomaly fields without referencing to a full-field weather system. For example, two anomalous lows may look similar in anomaly maps but could be associated with very different weather systems, such as a midlatitude cyclone versus a tropical cyclone. On the other hand, an anomalous system will provide more insightful details about structure. Therefore, the anomaly method cannot replace the full-field method but serves as a good supplement. By referencing full-field and anomaly weather maps together, one will have a fuller picture of an event and a deeper understanding of the underlying physical processes.

From the examples shown in the "Model prediction" section, we can see that the benefit of an anomaly-based model stems mainly from its simplification. Simplification enables a model to focus on main causes and identify the main controlling factors of a weather system and produce a more accurate forecast (e.g., the GBAM example). Simplification amplifies forecast signals and increases the predictability of a predictand. Simplification also makes a model more affordable in computing resources but still with reasonable accuracy (e.g., the anomaly GCM example). On the other hand, simplification means incompleteness for a model, which will surely result in errors. The technical difficulty in decomposing a complex dynamic model is another barrier to using anomaly model. For a state of the art NWP model with full physics, it is almost impossible or extremely difficult to decompose it into climate and anomaly components. Partial decomposition within a model may be possible to simplify nonlinear processes and focus on the main causes to improve a forecast. Finally, due to the reduction of complexity and nonlinearity, a simplified anomaly model will be less sensitive to changes in initial conditions and model physics. Therefore, it might not be able to produce rare solutions with low probability. Therefore, an anomaly model might not be suitable for an ensemble prediction whose aim is to capture a full spectrum of all possibilities. More research is apparently needed in the study of the anomaly model.

Summary

To explore whether there is a better approach than the traditional synoptic analysis for weather analysis and forecasting, an anomaly-based method has been systematically compared with the full-field-based method for the last decade. The findings have been individually published in more than 30 journal articles. Evidence from these studies has demonstrated the superiority of the anomaly approach over a full-field approach in the following four general aspects: depiction of weather systems using anomaly weather maps, anomaly forecasts, diagnostic parameters and model prediction. To promote the use and further discussion of the anomaly approach, this article has reviewed those findings.

For weather system depiction, anomaly weather maps have been applied to all kinds of weather extremes including heat waves, cold surges, heavy rainfall, freezing rain, fog, convection, tropical cyclones, and fire weather as well as air pollution. It is found that anomaly weather maps have at least five advantages compared to full-field weather maps: 1) less vagueness in visually connecting the location of a weather event with the associated meteorological conditions, 2) clearer and more complete depictions of the vertical structures of a weather system, 3) easier observation of the time and spatial evolution of a weather event as well as its interaction and connection with other weather systems far and near, 4) simplification of conceptual models by unifying different weather systems or even completely opposite

weather phenomena into one pattern, and 5) extension of model forecast length due to earlier detection of signals or predictors. Anomaly weather maps can also be used to compare different models' performance as a verification tool. Whether anomaly-based verification is systematically better than full-field-based verification needs to be studied.

The anomaly forecast has been proposed and widely accepted by the weather forecasting community over the last two decades. Comparing a forecast to local climatology can provide unique information about the significance level of an upcoming event. By further combining anomaly forecast with ensemble forecasts, an anomaly forecast can provide not only the significance level of an upcoming event but also the confidence level of the forecast itself. With both the event significance and forecast confidence information, an SII can be calculated through a societal impact matrix. The SII is an indicator of situational awareness level to raise a user's awareness of potential societal impact. Establishing the meaning and physical understanding of an SII value needs a large number of cases, where ensemble reforecasting dataset has a great potential to contribute.

For diagnostic parameters, two examples are given: an anomalous convective instability index for convective storms, and seven vorticity- and divergence-related parameters for heavy rain areal coverage. They generally performed better when a full field was replaced by an anomalous field. This result also showed that for multivariable parameters, a hybrid version (i.e., anomaly for one variable and full field for another) often performed better than a pure-anomaly version (i.e., anomaly for all variables).

For model prediction, the anomaly version of a beta-advection model with no physics was used as a demonstration. It consistently outperformed its full-field version in predicting tropical cyclone tracks, especially unusual tracks. This success is believed to be attributable to two reasons: 1) the anomaly model focuses on the main causes rather than secondary causes, and 2) the steering flow level can be exactly determined in the anomaly model. An anomaly model also makes it easier to test different roles played by surrounding disturbances and the climatic environment in determining a tropical cyclone's track. Similar to the diagnostic parameter study, the beta-advection model study also showed that a hybrid version performed better than a pure-anomaly version. When the full field was used for the steering flow and the anomaly flow was used for the vorticity and beta effect, it produced the best track forecasts. In addition, a historical work related to anomaly GCM models for long-range weather forecasts has also been reviewed.

Advantages and disadvantages always come in pairs. Three caveats with the anomaly approach were discussed. First, local and mesoscale weather could fall through the cracks in anomaly maps and anomaly forecasts due to the limitation in spatial and temporal resolution of available data, especially climatology. Second, a full meteorological interpretation and understanding of anomalous systems needs the use of full-field weather systems. Without understanding the full field weather system, an anomaly alone could sometimes be misleading. Third, anomalization of a complex dynamic model with full physics is extremely difficult if it is not impossible. Application of the anomaly approach to simple dynamical and statistical models is more feasible. Due to the reduction of model complexity and nonlinearity, an anomaly model might not be suitable for ensemble prediction purposes. More work needs to be done to advance this relatively new area of anomaly-based weather analysis and forecasting, which is the purpose of this review.

Acknowledgments. The first author (WQ) was supported by the Pearl River Talent Recruitment Program (2019ZT08G669) and the National Natural Science Foundation of China (U1811464 and 41775067). We thank Ms. Mary Hart of NCEP for checking the English language of the initial manuscript. The constructive comments and suggestions from the two anonymous reviewers and the editor Dr. Fovell have significantly improved the second version of the manuscript.

References

Alcott, T., R. Graham, N. Hosenfeld, C. Kahler, and R. Grumm, 2014: Using the ensemble situational awareness table: How I learned to stop worrying and love the global ensembles. *VLab Forum*, Silver Spring, MD, NWS, https://vlab.ncep.noaa.gov/documents/10157/137122/Alcott_19Feb14_ensembles.

Bevan, M., 2017: Impact based warning—Does it work? *Regional Workshop on Impact-Based Forecasts in RA II*, Seoul, South Korea, WMO–KMA, www.wmo.int/pages/prog/amp/pwsp/documents/1-4-1_MarkBEVAN_UK.pdf.

Chao, J. P., X. Wang, Y. Chen, and L. Wang, 1986: Monthly and seasonal numerical forecasts by using the anomaly ocean-atmosphere coupled filtered model. *Adv. Atmos. Sci.*, **3**, 139–149, https://doi.org/10.1007/BF02682548.

Chen, Y., Q. Hu, Y. M. Yang, and W. H. Qian, 2017: Anomaly based analysis of extreme heat waves in eastern China during 1981–2013. *Int. J. Climatol.*, **37**, 509–523, https://doi.org/10.1002/joc.4724.

Dee, D. P., and Coauthors, 2011: The ERA-Interim reanalysis: Configuration and performance of the data assimilation system. *Quart. J. Roy. Meteor. Soc.*, **137**, 553–597, https://doi.org/10.1002/qj.828.

Du, J., R. H. Grumm, and G. Deng, 2013: Ensemble anomaly forecasting approach to predicting extreme weather demonstrated by extremely heavy rain event in Beijing. *Chin. J. Atmos. Sci.*, **38**, 685–688.

——, and Coauthors, 2018: Ensemble methods for meteorological predictions. *Handbook of Hydrometeorological Ensemble Forecasting*, Q. Duan et al., Eds., Springer, 1–52.

Economou, T., D. B. Stephenson, J. C. Rougier, R. Neal, and K. Mylne, 2016: On the use of Bayesian decision theory for issuing natural hazard warnings. *Proc. Roy. Soc. London*, **472A**, 20160295, https://doi.org/10.1098/rspa.2016.0295.

Graham, R. A., and R. H. Grumm, 2010: Utilizing normalized anomalies to assess synoptic-scale weather events in the western United States. *Wea. Forecasting*, **25**, 428–445, https://doi.org/10.1175/2009WAF2222273.1.

Grahame, N., 2000: The development of meteorology over the last 150 years as illustrated by historical weather charts. *Weather*, **55**, 108–117, https://doi.org/10.1002/j.1477-8696.2000.tb04041.x.

Grumm, R. H., 2011a: The central European and Russian heat event of July–August 2010. *Bull. Amer. Meteor. Soc.*, **92**, 1285–1296, https://doi.org/10.1175/2011BAMS3174.1.

——, 2011b: New England record maker rain event of 29–30 March 2010. *Electron. J. Oper. Meteor.*, **12** (4), www.nwas.org/ej/pdf/2011-EJ4.pdf.

——, and R. Hart, 2001: Standardized anomalies applied to significant cold season weather events: Preliminary findings. *Wea. Forecasting*, **16**, 736–754, https://doi.org/10.1175/1520-0434(2001)016<0736:SAATSC>2.0.CO;2.

——, J. D. Ross, and P. G. Knight, 2005: Examining severe weather events using reanalysis datasets. Preprint, *17th Conf. on Numerical Weather Prediction/21st Conf. on Weather Analysis and Forecasting*, Washington DC., Amer. Meteor. Soc., P1.87, https://ams.confex.com/ams/pdfpapers/94351.pdf.

Guo, Y., and J.-P. Chao, 1984: Simplified dynamical anomaly model for long-range numerical forecasts. *Adv. Atmos. Sci.*, **1**, 30–39, https://doi.org/10.1007/BF03187614.

Hamill, T. M., G. T. Bates, J. S. Whitaker, D. R. Murray, M. Fiorono, T. J. Galarneau Jr., Y. Zhu, and W. Lapenta, 2013: NOAA's second-generation global medium-range ensemble reforecast dataset. *Bull. Amer. Meteor. Soc.*, **94**, 1553–1565, https://doi.org/10.1175/BAMS-D-12-00014.1.

Hart, R. E., and R. H. Grumm, 2001: Using normalized climatological anomalies to rank synoptic scale events objectively. *Mon. Wea. Rev.*, **129**, 2426–2442, https://doi.org/10.1175/1520-0493(2001)129<2426:UNCATR>2.0.CO;2.

Huang, J., J. Du, and W. H. Qian, 2015: A comparison between a generalized beta–advection model and a classical beta–advection model in predicting and understanding unusual typhoon tracks in eastern China seas. *Wea. Forecasting*, **30**, 771–792, https://doi.org/10.1175/WAF-D-14-00073.1.

Jiang, N., W. H. Qian, J. Du, R. H. Grumm, and J. L. Fu, 2016: A comprehensive approach from the raw and normalized anomalies to the analysis and prediction of the Beijing extreme rainfall on July 21, 2012. *Nat. Hazards*, **84**, 1551–1567, https://doi.org/10.1007/s11069-016-2500-0.

Junker, N. W., R. H. Grumm, R. Hart, L. F. Bosart, K. M. Bell, and F. J. Pereira, 2008: Use of standardized anomaly fields to anticipate extreme rainfall in the mountains of Northern California. *Wea. Forecasting*, **23**, 336–356, https://doi.org/10.1175/2007WAF2007013.1.

——, M. J. Brennan, F. Pereira, M. J. Bodner, and R. H. Grumm, 2009: Assessing the potential for rare precipitation events with standardized anomalies and ensemble guidance at the Hydrometeorological Prediction Center. *Bull. Amer. Meteor. Soc.*, **90**, 445–454, https://doi.org/10.1175/2008BAMS2636.1.

Lamberson, W., T. Alcott, and C. Kahler, 2015: The ensemble situational awareness table: Overview and future enhancements. *VLab Forum*, Silver Spring, MD, NWS, https://vlab.ncep.noaa.gov/documents/10157/137122/ESAT_Lamberson_18Nov15.pdf.

Miyakoda, K., and J.-P. Chao, 1982: Essay on dynamical long-range forecasts of atmospheric circulation. *J. Meteor. Soc. Japan*, **60**, 292–308, https://doi.org/10.2151/jmsj1965.60.1_292.

Peixoto, J. P., and A. H. Oort, 1992: *Physics of Climate*. AIP Press, 520 pp.

Qian, W. H., 2012a: *Principles of Medium to Extended Range Weather Forecasts*. China Science Press, 199 pp.

——, 2012b: Planetary-scale and regional-scale anomaly signals for persistent drought events over southwest China. *Chin. J. Geophys.*, **55**, 1462–1471, https://doi.org/10.6038/J.ISSN.0001-5733.2012.05.004.

——, 2017: *Temporal Climatology and Anomalous Weather Analysis*. Springer, 687 pp.

——, and H. Y. Liang, 2012: Propagation of planetary-scale zonal mean wind anomalies and polar oscillations. *Chin. Sci. Bull.*, **57**, 2606–2614, https://doi.org/10.1007/s11434-012-5168-1.

——, and Z. J. Zhang, 2012: Precursors to predict low-temperature freezing-rain events in southern China. *Chin. J. Geophys.*, **55**, 1501–1512, https://doi.org/10.6038/J.ISSN.0001-5733.2012.05.007.

——, and M. Jiang, 2014: Early signals of synoptic-scale atmospheric anomalies associated with the summer low temperature events in northeast China. *Meteor. Atmos. Phys.*, **124**, 33–46, https://doi.org/10.1007/s00703-013-0306-0.

——, and J. Huang, 2019: Applying the anomaly-based weather analysis on Beijing severe haze episodes. *Sci. Total Environ.*, **647**, 878–887, https://doi.org/10.1016/j.scitotenv.2018.07.408.

——, X. L. Shan, H. Y. Liang, J. Huang, and C. H. Leung, 2014: A generalized beta-advection model to improve unusual typhoon track prediction by decomposing total flow into climatic and anomalous flows. *J. Geophys. Res. Atmos.*, **119**, 1097–1117, https://doi.org/10.1002/2013JD020902.

——, J. Du, X. L. Shan, and N. Jiang, 2015: Incorporating the effects of moisture into a dynamical parameter: Moist vorticity and moist divergence. *Wea. Forecasting*, **30**, 1411–1428, https://doi.org/10.1175/WAF-D-14-00154.1.

——, J. Huang, and J. Du, 2016a: Examination of Hurricane Sandy's (2012) structure and intensity evolution from full-field and anomaly-field analyses. *Tellus*, **68A**, 29029, https://doi.org/10.3402/tellusa.v68.29029.

——, N. Jiang, and J. Du, 2016b: Anomaly-based weather analysis versus traditional total-field-based weather analysis for depicting regional heavy rain events. *Wea. Forecasting*, **31**, 71–93, https://doi.org/10.1175/WAF-D-15-0074.1.

——, ——, and ——, 2016c: Reply to "Comments on 'Incorporating the effects of moisture into a dynamical parameter: Moist vorticity and moist divergence.'" *Wea. Forecasting*, **31**, 1397–1405, https://doi.org/10.1175/WAF-D-16-0111.1.

——, K. J. Wu, and J. C. H. Leung, 2016d: Three-dimensional structure and long-term trend of heat wave events in western Eurasia revealed with an anomaly-based approach. *Int. J. Climatol.*, **36**, 4315–4326, https://doi.org/10.1002/joc.4634.

——, T. T. Yu, and J. Du, 2016e: A unified approach to trace surface heat and cold events by using height anomaly. *Climate Dyn.*, **46**, 1647–1664, https://doi.org/10.1007/s00382-015-2666-2.

——, J. C. H. Leung, Y. L. Chen, and S. Y. Huang, 2019a: Applying anomaly-based weather analysis to the prediction of low visibility associated with the coastal fog at Ningbo-Zhoushan Port in East China. *Adv. Atmos. Sci.*, **36**, 1060–1077, https://doi.org/10.1007/s00376-019-8252-5.

——, ——, W. M. Luo, J. Du, and J. D. Gao, 2019b: An index of anomalous convective instability to detect tornadic and hail storms. *Meteor. Atmos. Phys.*, **131**, 351–373, https://doi.org/10.1007/s00703-017-0576-z.

Root, B. V., P. G. Knight, G. S. Young, S. Greybush, R. H. Grumm, R. Holmes, and J. D. Ross, 2007: A fingerprinting technique for major weather events. *J. Appl. Meteor. Climatol.*, **46**, 1053–1066, https://doi.org/10.1175/JAM2509.1.

Suri, D., 2015: The UK National Severe Weather Warning Service—Guidance Unit perspective. *Using ECMWF Forecasts 2015*, Reading, United Kingdom, ECMWF, www.ecmwf.int/sites/default/files/elibrary/2015/13426-uk-national-severe-weather-warning-service-guidance-unit-perspective.pdf.

Van den Dool, H., 2007: *Empirical Methods in Short-Term Climate Prediction*. Oxford University Press, 215 pp.